Journal of X-Ray Science and Technology xx (20xx) x–xx
DOI 10.3233/XST-17284
IOS Press

Three novel accurate pixel-driven projection methods for 2D CT and 3D EPR imaging

Zhiwei Qiao[a,d,*], Gage Redler[b], Zhiguo Gui[c], Yuhua Qian[a], Boris Epel[d] and Howard Halpern[d]

[a]*School of Computer and Information Technology, Shanxi University, Taiyuan, Shanxi, China*
[b]*Department of Radiation Oncology, Rush University Medical Center, Chicago, IL, USA*
[c]*School of Information and Communication Engineering, North University of China, Taiyuan, Shanxi, China*
[d]*Department of Radiation and Cellular Oncology, The University of Chicago, Chicago, IL, USA*

Received 30 March 2017
Revised 06 July 2017
Accepted 04 August 2017

Abstract.
OBJECTIVES: This work aims to explore more accurate pixel-driven projection methods for iterative image reconstructions in order to reduce high-frequency artifacts in the generated projection image.
METHODS: Three new pixel-driven projection methods namely, small-pixel-large-detector (SPLD), linear interpolation based (LIB) and distance anterpolation based (DAB), were proposed and applied to reconstruct images. The performance of these methods was evaluated in both two-dimensional (2D) computed tomography (CT) images via the modified FORBILD phantom and three-dimensional (3D) electron paramagnetic resonance (EPR) images via the 6-spheres phantom. Specifically, two evaluations based on projection generation and image reconstruction were performed. For projection generation, evaluation was using a 2D disc phantom, the modified FORBILD phantom and the 6-spheres phantom. For image reconstruction, evaluations were performed using the FORBILD and 6-spheres phantom. During evaluation, 2 quantitative indices of root-mean-square-error (RMSE) and contrast-to-noise-ratio (CNR) were used.
RESULTS: Comparing to the use of ordinary pixel-driven projection method, RMSE of the SPLD based least-square algorithm was reduced from 0.0701 to 0.0384 and CNR was increased from 5.6 to 19.47 for 2D FORBILD phantom reconstruction. For 3D EPRI, RMSE of SPLD was also reduced from 0.0594 to 0.0498 and CNR was increased from 3.88 to 11.58. In addition, visual evaluation showed that images reconstructed in both 2D and 3D images suffered from high-frequency line-shape artifacts when using the ordinary pixel-driven projection method. However, using 3 new methods all suppressed the artifacts significantly and yielded more accurate reconstructions.
CONCLUSIONS: Three proposed pixel-driven projection methods achieved more accurate iterative image reconstruction results. These new and more accurate methods can also be easily extended to other imaging modalities. Among them, SPLD method should be recommended to 3D and four dimensional (4D) EPR imaging.

Keywords: Accurate pixel-driven projection, iterative image reconstruction, computed tomography, electron paramagnetic resonance imaging

1. Introduction

Computed tomography (CT), magnetic resonance imaging (MRI) and electron paramagnetic resonance (EPR) imaging (EPRI) [1] are all imaging modalities that rely on some form of image reconstruction algorithms to generate images from acquired data. EPRI has similar physics with MRI,

---

[*] Corresponding author: Dr. Zhiwei Qiao, School of Computer and Information Technology, Shanxi University, Taiyuan, Shanxi 030006, China. E-mail: zqiao@sxu.edu.cn.

but has similar image reconstruction algorithms with CT for the data for EPRI is also spatial-projection data rather than K-space data. So, knowledge and insights obtained in CT reconstruction algorithms may be explicitly and easily extended to EPRI. 2D parallel beam CT reconstruction is the problem of 2D inverse Radon transform; 3D and 4D EPRI reconstruction are the problems of 3D and 4D inverse Radon transform, respectively; So EPRI reconstruction may be regarded as the high dimensional extension of 2D parallel beam CT as per reconstruction algorithm.

For discrete-to-discrete 3D EPRI imaging model, the key problem for modeling the forward process, i.e. the *projection* process, is the calculation of the imaged object area integral on a plane [2]. The projection method we used in our previous total variation (TV) minimization algorithm for EPRI [3] is plane-driven which is the 3D extension of ray-driven technic in 2D CT. This method is exact but overly complicated, requiring the calculation of the intersecting area of a plane with a cube in 3D space [2]. For 4D EPRI, the key will be the calculation of the intersecting volume of a 4D-hyperplane with a 4D-hypercube [4, 5]. Clearly, the plane-driven or the hyperplane-driven methods extended from the ray-driven projection method in 2D CT are too complicated to be efficient and practical. Thus it is reasonable to turn to back to 2D parallel beam CT, to find a simpler yet accurate approach for computing projections that can be later easily extended to EPRI.

Now that ray-driven is not suitable for extended use in EPRI, we should investigate the other projection methods in CT and evaluate their extension capabilities in EPRI. To our knowledge, there are 3 main types of projection method in 2D CT: pixel-driven [6], ray-driven [7–10] and distance-driven [11–13]. Pixel-driven projection method tends to be simpler in principle and is potentially easy to extend to high dimensional problems but often result in high-frequency artifacts in the generated projections [3, 11, 14]. Ray-driven and distance-driven methods generate projections very accurately and avoid these high-frequency artifacts. However, these methods are difficult to be extended to 3D or 4D EPR imaging. Difficulty of the extension of distance-driven is that it still needs to calculate the intersection area of a plane and a cuboid for 3D case and to calculate the intersection volume of a hyper-plane and a hyper-cuboid for 4D case. Thus, the optimal choice appears to be developing accurate pixel-driven projection methods to fully employ their property of easy-to extend.

A so-called splatting technique may help to reduce the artifacts [15, 16] for pixel-driven method but this technique is computationally complex and cannot be readily extended to other imaging modalities. The general approach to splatting is calculating the analytical footprint of a pixel (voxel) and then distributing or splatting the footprint to the detector cells. The calculation of the pixel footprints is time-consuming. Some approaches involve pre-calculating and storing the footprint [16] and some use separable footprints [15] to speed up the calculation. However, these approaches may require huge amounts of memory to store pre-calculated footprints or may introduce additional errors by approximating the footprint as a combination of separable footprints. In addition, the use of an analytical footprint requires imaging modality specific formalisms and thus lowers the extension capability of these methods. In 4D EPRI, the key would be to calculate the footprint of a hypercube, which is exceedingly complex.

In this work, we analyze the root reason of high-frequency artifacts introduced by the ordinary pixel-driven projection method firstly. And then we propose 3 new, simple and accurate pixel-driven projection methods that can be easily extended to other imaging modalities, such as EPRI. These methods include small-pixel-large-detector (SPLD), linear interpolation based (LIB) and distance anterpolation based (DAB) projection methods.

In Section 2, we begin by introducing 2 interpolation and 2 anterpolation approaches that will be used in the proposed methods. We analyze the producing reason of high-frequency artifacts introduced by the ordinary pixel-driven method and then propose the 3 new accurate pixel-driven projection methods specifically designed to avoid such artifacts. In Section 3, we verify and evaluate the 3 new pixel-driven projection methods in 2D CT by comparisons of the generated projections and the corresponding iterative reconstructions. We also extend the first proposed pixel-driven method, i.e. SPLD to 3D EPRI and perform evaluation studies. Finally, brief discussions and conclusions are given in Section 4.

2. Methods

In this section, we propose and discuss 3 new accurate pixel-driven projection methods. Since these methods rely on interpolation or anterpolation techniques, we present these concepts firstly.

2.1. Interpolation VS anterpolation

Interpolation is a method for estimating unknown values of a function based on known values of the function near the point of interest. In projection and backprojection operations, interpolation is frequently used. Usually, linear interpolation is extensively used for it is simple but accurate enough. The opposite operation of linear interpolation is the distribution of a known function value to the two adjacent unknown function values. In [11], the authors named such an operation linear *anterpolation*.

For distance-driven projection methods, a special interpolation approach is used. A pixel and a ray are treated as a square and a strip, respectively. A 1D kernel operation [11] is used to determine the value of the intersection of a ray and an image-row-centerline based on the overlap length of the ray and the pixels on the image-row-centerline. The kernel operation is a special interpolation approach based on the assumption that each function value is from a line-segment rather than a point. We will refer to this as *distance interpolation* and the opposite operation will be referred to as *distance anterpolation*.

2.1.1. Linear interpolation

If there is a function $f(x)$, for which two adjacent values are known to be $f(a)$ and $f(b)$, then $f(c)$ may be estimated by linear interpolation as shown in Equation (1).

$$f(c) = \frac{b-c}{b-a} f(a) + \frac{c-a}{b-a} f(b) \tag{1}$$

2.1.2. Linear anterpolation

The main idea is to distribute a known value to the two adjacent points, which is expressed mathematically in Equation (2). Here, symbol ‘+ = ’ means to add the right-hand-side vaule to the left-hand-side variable (the same below).

$$\begin{cases} f(a) += \frac{b-c}{b-a} f(c) \\ f(b) += \frac{c-a}{b-a} f(c) \end{cases} \tag{2}$$

2.1.3. Distance interpolation

Conceptually, distance interpolation and anterpolation assume that a function-value comes from a line segment rather than a single point, i.e. the function is piecewise constant. For standard linear interpolation, the estimated intermediate value is derived from the value at two adjacent points, but for distance interpolation, the estimated sample value may be derived from one, two or more samples, depending on the length of the line segment corresponding to the unknown sample. Figure 1 is the schematic representation for three distance interpolation cases. The corresponding distance interpolation expressions are shown in Equations (3)–(5).

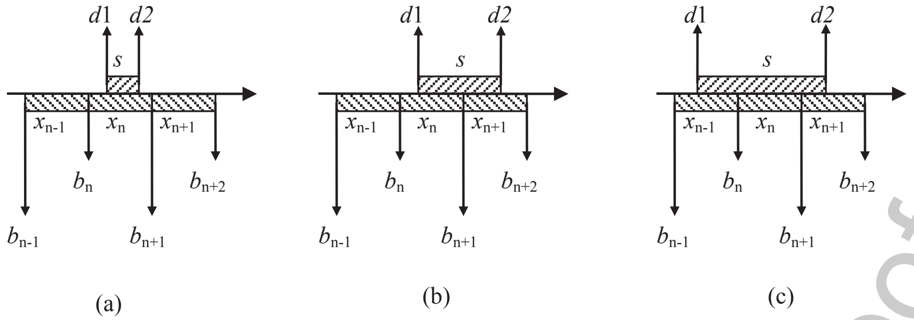

Fig. 1. Three cases of distance interpolations: the case in which the width of the unknown sample (a) belongs to one known sample, (b) crosses two known samples and (c) crosses three samples. $d1$ and $d2$ are the boundaries of the unknown sample S. b_i and b_{i+1} are the boundaries of the known sample x_i.

$$f(s) = f(x_n) \tag{3}$$

$$f(s) = \frac{b_{n+1} - d_1}{d_2 - d_1} f(x_n) + \frac{d_2 - b_{n+1}}{d_2 - d_1} f(x_{n+1}) \tag{4}$$

$$f(s) = \frac{b_n - d_1}{d_2 - d_1} f(x_{n-1}) + \frac{b_{n+1} - b_n}{d_2 - d_1} f(x_n) + \frac{d_2 - b_{n+1}}{d_2 - d_1} f(x_{n+1}) \tag{5}$$

From Equations (3) to (5), it can be seen that distance interpolation computes the sum of all the known samples overlapping with the unknown weighted by the overlap length divided by the length of the unknown sample.

2.1.4. Distance anterpolation

Distance anterpolation distributes a known function value to the overlapping unknown function values. The most important point is that distance anterpolation may distribute a known value to more than 2 samples if the length of the known sample is long enough to across more than 2 samples. Figure 1 can also be the schematic representation of the three distance anterpolation cases. Now, the problem is to distribute the known sample $f(s)$ to the function $f(x)$. For the 3 different cases depicted in Fig. 1, the known sample may be distributed over 1, 2 and 3 samples, respectively. Equations (6)–(8) are the mathematical expressions for the 3 cases of distance anterpolation.

$$f(x_n) += \frac{d_2 - d_1}{b_{n+1} - b_n} f(s) \tag{6}$$

$$f(x_n) += \frac{b_{n+1} - d_1}{b_{n+1} - b_n} f(s) \qquad f(x_{n+1}) += \frac{d_2 - b_{n+1}}{b_{n+2} - b_{n+1}} f(s) \tag{7}$$

$$f(x_{n-1}) += \frac{b_n - d_1}{b_n - b_{n-1}} f(s) \quad f(x_n) += f(s) \quad f(x_{n+1}) += \frac{d_2 - b_{n+1}}{b_{n+2} - b_{n+1}} f(s) \tag{8}$$

From Equations (6) to (8), it can be seen that distance anterpolation is the distribution of the known sample value to the unknown sample values weighted by the overlap length divided by the length of the unknown sample.

2.1.5. Interpolation and anterpolation operators

We name some operators corresponding to the interpolation or anterpolation approaches discussed above. We refer to linear interpolation, anterpolation, distance interpolation and anterpolation as *interp_lin*, *anterp_lin, interp_dis* and *anterp_dis*, respectively.

2.2. The ordinary pixel-driven projection method

Here we present the ordinary pixel-driven projection method. Take 2D parallel beam CT to be example. The 2D pixel grid is $f(m, n)$ with size $N \times N$; the projection at a specific angle is $p(k)$ with size $N \times 1$; the size of each pixel and detector cell both has unit length. The schematic diagram of pixel-driven projection is shown in Fig. 2. The algorithm is summarized in Algorithm 1.

Algorithm 1: The ordinary pixel-driven.

```
for $m = 1: N$
  for $n = 1: N$
    Calculate the coordinates $(x, y)$ of pixel $(m, n)$ in the imaging coordinate system
    Calculate the projection address $t$ using the equation: $t = x\cos\theta + y\sin\theta$
    Anterpolate the projected pixel value to adjacent detector elements, i.e. $p += anterp\_lin(t, p)$
  end for $n$
end for $m$
```

2.3. Three new accurate pixel-driven projection methods

It is known that pixel-driven projection method introduces artifacts in projections. Pixel-driven projection relies on linear *anterpolation*. This suggests that the reason for producing these artifacts may be related to the use of linear anterpolation. Nyquist sampling theory requires that the sampling frequency should be equal to or more than double the highest frequency contained in the signal. Supposing that the projection signal is the destination signal and that the image is the source signal, the high frequency artifacts arising when using pixel-driven projection methods may be removed by ensuring that the pixel size is less than or equal to 1/2 of the detector element size, in order to satisfy the Nyquist condition. Therefore, re-sampling the image and applying appropriate pixel weighting factors should prevent loss of accuracy and avoid high-frequency artifacts. This is the basis of the first new accurate *small-pixel-large-detector* (SPLD) pixel-driven method.

Since linear anterpolation introduces artifacts, making use of linear interpolation instead for pixel-driven projection may be advantageous. Rather than projecting the pixels one by one and anterpolating

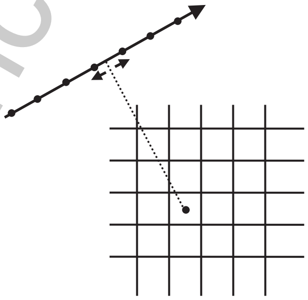

Fig. 2. The ordinary pixel-driven projection: each pixel value is projected to the detector by linear anterpolation.

the projected value to nearby detector elements, we propose to project the pixels row by row (or column by column). Projecting all of the pixels in a row to the detector gives signal values at all of the projection addresses for these pixels. Signal values at the actual detector cells can then be obtained using linear interpolation. The final projection can be obtained by repeating the process row by row and calculating the weighted summation of the intermediate projections coming from the row-actions. Thus we arrive at the second new accurate pixel-driven method: *linear interpolation based* (LIB) pixel-driven method.

Motivated by the concept of distance anterpolation, we implement pixel-driven projection but replace the standard linear anterpolation with distance anterpolation. This is the third new accurate pixel-driven method: *distance anterpolation based* (DAB) pixel-driven method.

The algorithms for these three new methods are summarized below in algorithms 2–4. Figure 3 is the schematic diagrams of the 3 new accurate pixel-driven projection methods.

Algorithm 2: SPLD pixel-driven. Each pixel subdivided into 4 sub-pixels.

```
for $m = 1: N$
  for $n = 1: N$
    Divide the pixel into 4 small pixels, $f_1, f_2, f_3, f_4$ with the same value $f(m, n)$
    for $i = 1 : 4$
      Calculate the coordinates $(x, y)$ of pixel $f_i$ in the imaging coordinate system
      Calculate the projection address $t$ using the equation: $t = x\cos\theta + y\sin\theta$
      Anterpolate the pixel value $f_i$ to adjacent detector elements, multiply by
      weighting factor and add to projection, i.e. $p += anterp\_lin(t, p) \times 1/4$
    end for $i$
  end for $n$
end for $m$
```

2.4. The ordinary pixel-driven backprojection method

In the Result part, we will use the least square algorithm to evaluate the three proposed projection methods. For the other iteratively used operation is the backprojection operation, we present the ordinary pixel-driven backprojection method in Algorithm 5. Note that pixel-driven backprojection method is accurate. Take 2D parallel beam CT to be example. The 2D pixel grid is $f(m, n)$ with size

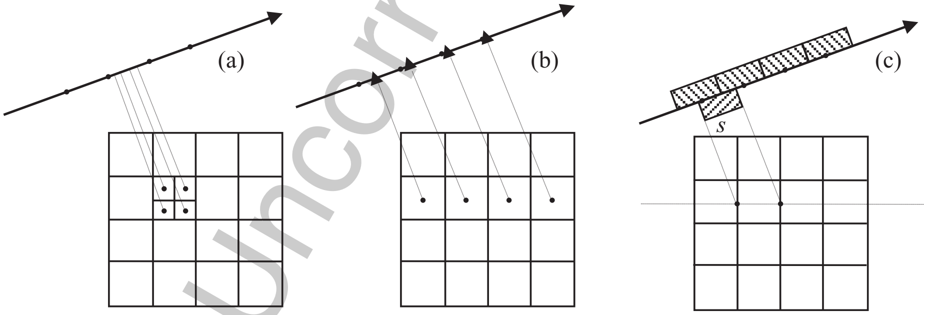

Fig. 3. The schematic diagrams of the 3 new accurate pixel-driven projection methods using a 4 × 4 image example. (a) *SPLD pixel-driven*: Each pixel is subdivided into 4 small pixels, which are projected to the detector. The projection is updated by use of linear anterpolation to the projection point of every small pixel. *(b) LIB pixel-driven:* Every row is projected onto the detector to get the values on the small triangle positions. Then the values on the detector cells, i.e. the dot positions may be obtained by linear interpolation. (c) *DAB pixel-driven*: Using the distance anterpolation approach on every pixel during the traditional pixel-driven projection process. Here, s is the projected sample of a pixel.

Algorithm 3: LIB pixel-driven.

```
Calculate the coordinates of the projection-measurement indices $h_k, k = 1, 2, 3, \ldots, N$
for $m = 1$:N
    Calculate all the projection addresses $t_1, t_2, \ldots, t_N$ of the $m$th row pixels, getting a projection signal$p_t(t_i) = f(m, i), i = 1, 2, \ldots, N$
    for $k = 1$:N
        Linearly interpolate to obtain the row-projection: $p_0(h_k) = \mathrm{int}\,erp\_lin(h_k, p_t)$
    end for $k$, $p_0$ represents the contribution to the final projection from a single row.
    Update the projection $p$ with the weighted row-projection, $p = p + p_0 \times w_{len}$
end for $m$
```

Algorithm 4: DAB pixel-driven. Using row-action.

```
for $m = 1$: $N$
    for $n = 1$: $N$
        Calculate the coordinates $(x_1, y_1)$ and $(x_2, y_2)$ of the two boundary points of pixel $(m, n)$ in the imaging coordinate system
        Calculate the projection addresses $t_1$ and $t_2$ of the two boundary points using the equation: $t = x\cos\theta + y\sin\theta$.
        Define a sample $s$ that spans the line segment $[t_1, t_2]$ with a value $p(s) = f(m, n)$.
        Anterpolate the sample value $p(s)$ to projection $p$ using the distance anterpolation approach and weight its contribution using the length-weighted factor, $p+ = anterp\_dis(s, p) \times w_{len}$
    end for $n$
end for $m$
```

Algorithm 5: The ordinary pixel-driven backprojection.

```
for $m = 1$: $N$
    for $n = 1$: $N$
        Calculate the coordinates $(x, y)$ of pixel $(m, n)$ in the imaging coordinate system
        Calculate the projection address $t$ using the equation: $t = x\cos\theta + y\sin\theta$
        Get the value at the projection address, i.e. $f(m, n) = \mathrm{int}\,erp\_lin\,(t, p)$.
    end for $n$
end for $m$
```

$N \times N$; the projection at a specific angle is $p(k)$ with size $N \times 1$; the size of each pixel and detector cell both has unit length. The algorithm is summarized in Algorithm 5.

2.5. Accuracy-evaluation metrics

In order to verify, evaluate and compare the 3 new accurate pixel-driven projection methods integrally, we use root-mean-square-error (RMSE) as the metric. The RMSE is expressed in Equation (9).

$$RMSE = \sqrt{\frac{\sum_{i=1}^{N}(p_i - g_i)^2}{N}} \tag{9}$$

where, p and g are the generated (reconstructed) signal and the ideal signal, respectively. The signals both have N points indexed by i. We will use the metric to measure the projection error and the reconstruction error.

To quantitatively evaluate the reconstruction quality focusing on several region of interest (ROI), we use the contrast-to-noise ratio (CNR) as metric [17] expressed in Equation (10).

$$\mathrm{CNR} = \frac{2\,|m_s - m_b|}{\delta_s + \delta_b} \tag{10}$$

where, m_{s} and m_{b} are the mean values of the vectorized signal-image s and background-image b, respectively. δ_{s} and δ_{b} are the standard deviation values of the vectorized sinal-image and background-image, respectively. Generally, if there is a vectorized image f of N pixels (voxels), the mean value m_{f} and standard deviation δ_{f} are expressed in Equations (11) and (12), respectively.

$$m_{\mathrm{f}} = \frac{1}{N}\sum_{\mathrm{n}=1}^{N} f_{\mathrm{n}} \tag{11}$$

$$\delta_{\mathrm{f}} = \sqrt{\frac{1}{N-1}\sum_{n=1}^{N}(f_{\mathrm{n}} - m_{\mathrm{f}})^2} \tag{12}$$

where, $f = [f_1, f_2, \ldots, f_{\mathrm{N}}]$ is the vectorized image-vector.

In the next section, we will use RMSE to evaluate the projection-generation accuracy and use RMSE and CNR to evaluate the reconstructed objects by use of the ordinary projection method and the SPLD, LIB and DAB methods.

2.5. Forward model for 3D EPR imaging

3D pulsed EPR imaging may be modeled as a 3D Radon transform [18]. Similar to the CT imaging model, the EPRI imaging model may also be separated into 2 types: continuous to continuous (C2C) and discrete to discrete (D2D) models.

2.5.1. C2C model

The 3D EPRI forward C2C model is the 3D Radon transform, shown in Equation (13) and Fig. 4 [18].

$$p(t,\varphi,\theta) = \iiint_{\Omega} f(x,y,z)\delta(x\cos\varphi\sin\theta + y\sin\varphi\sin\theta + z\cos\theta - t)dxdydz \tag{13}$$

where, $p(t,\varphi,\theta)$ is a 1D spatial projection signal at angle (φ,θ), $f(x,y,z)$ is a 3D object, δ is the standard Dirac function and $\Omega = R^3$. Using this formalism, a projection is the area integral of the 3D object on the corresponding plane: $t = x\cos\varphi\sin\theta + y\sin\varphi\sin\theta + z\cos\theta$.

2.5.2. D2D model

The 3D Radon transform is modeled using the D2D model by treating the object as a 3D voxel grid. The projections are also considered to be discrete. Suppose that the object is $t = x\cos\varphi\sin\theta + y\sin\varphi\sin\theta + z\cos\theta$. Then a measurement $p(i)$ may be denoted by Equation (14).

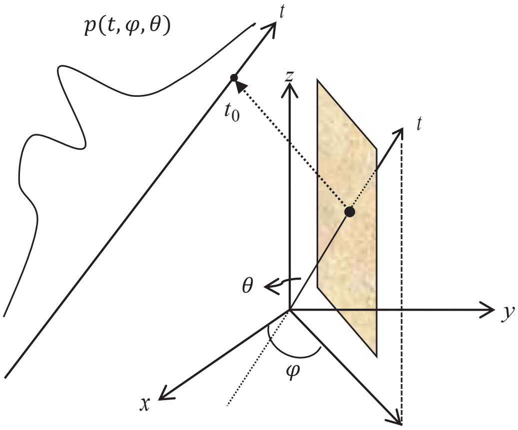

Fig. 4. The schematic diagram of 3D Radon transform. $p(t, \varphi, \theta)$ is a 1D spatial projection signal at angle (φ, θ), $f(x, y, z)$ is a 3D object, the δ function is the standard Dirac function and $\Omega = R^3$. The shaded parallelogram represents the plane $t_0 = x \cos\varphi \sin\theta + y \sin\varphi \sin\theta + z \cos\theta$. A measurement on the projection $p(t_0, \varphi, \theta)$ is the area integral of the function $f(x, y, z)$ on the plane represented by the parallelogram.

$$p(i) = \sum_{m} \sum_{n} \sum_{k} f(m, n, k) l(m, n, k) \tag{14}$$

where, $l(m, n, k)$ is the intersection area of the ith plane with the voxel $f(m, n, k)$ that projects to $p(i)$. Using Equation (14) results in the plane-driven method for 3D EPRI, which analogous to the ray-driven method in 2D CT.

3. Results

In this section, we perform 2 studies. One is for the evaluation of the 3 proposed pixel-driven methods in 2D CT. The other is for the evaluation of the SPLD projection method in 3D EPRI. In each study, we perform 2 evaluations: one to compare the projection accuracy and the other one to compare the accuracy of the corresponding iterative reconstruction. RMSE and CNR are used to perform quantitative evaluations, whereas the qualitative evaluations may be performed by visual observations of the signal-curves or images.

3.1. Application of the 3 new pixel-driven methods in 2D CT

3.1.1. Evaluation of projection methods on the simulated disc phantom

The mathematical phantom used is a large circle containing 4 smaller circles of different intensity (Fig. 5 (a)). The 2D pixel grid is of size 256 × 256 with each pixel being of unit area. The projection at a specific angle has 256 points with the sampling interval or detector cell being of unit length. The rotational center, i.e. the origin of the imaging coordinate system, is located at [128, 128]. To demonstrate the accuracy of these methods, we focus on the projection at the angle of 45°. We use the ordinary pixel-driven projection method and the 3 new pixel-driven projection methods to calculate the projection at 45° and compare them to the analytic projection which is regarded as the truth. The result of using the ordinary pixel-driven is shown in Fig. 5 (b). This method introduces obvious artifacts that resembling high-frequency noise. This phenomenon has been observed in previous studies [12]. Due to these artifacts, the traditional pixel-driven projection method is rarely used in image reconstruction.

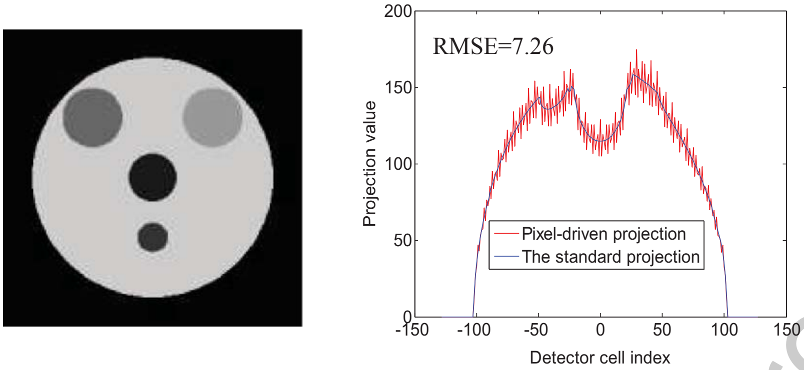

(a) (b)

Fig. 5. (a) The mathematical phantom. (b) The projection at 45° generated by use of the ordinary pixel-driven projection method and the analytic method.

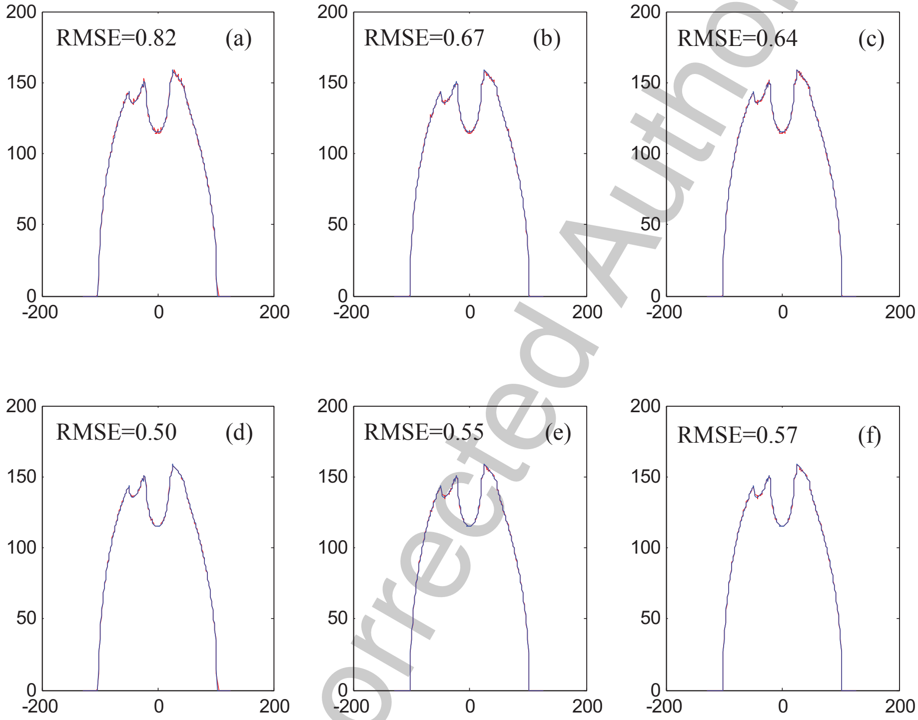

Fig. 6. Projections calculated using the 3 new pixel-driven projection methods (red) compared to the ideal analytic projection (blue). (a) to (d) show projections calculated using the SPLD method with re-sampling factors of 2,3,4 and 5, respectively. (e) shows the projection calculated using the LIB method and (f) shows the projection calculated using the DAB method.

The results of the 3 new pixel-driven projection methods are shown in Fig. 6. For the SPLD method, we used 4 different pixel re-sampling factors (2, 3, 4 and 5) to calculate the projections, the results of which are shown in Fig. 6 (a)-(d), respectively. A re-sampling factor of 2 means that we re-sampled image, so that the size of each pixel is reduced to 1/2 of the original size (i.e., half of the size of a detector element). Figure 6 (e) and (f) are projections calculated using the LIB and DAB projection methods, respectively.

Figure 6 shows that all of the new pixel-driven methods presented in this work are capable of yielding accurate projections. It can also be seen that, for the SPLD method, the higher the re-sampling factor is, the more accurate the projection is. This is depicted visually in Fig. 6 (a)-(d) as well as quantitatively using the RMSE (RMSE = 0.82, 0.67, 0.64 and 0.50 for re-sampling factors of 2, 3, 4, and 5, respectively). The RMSEs for the LIB and DAB methods are very close and are smaller than the SPLD method unless a re-sampling factor 5 is used. The SPLD method is more similar than the LIB and DAB methods to the traditional pixel-driven projection method. As discussed above, the traditional pixel-driven projection method is easily extended to other applications; therefore it is reasonable to suggest that SPLD is the optimal method to adopt for image reconstruction in other imaging modalities, such as 3D EPRI and 3D cone beam CT. Generally speaking, a re-sampling factor of 2 is sufficient for most image reconstruction applications. However, one may choose to use a higher factor to achieve higher accuracy in the calculated projections if necessary.

3.1.2. Evaluation of projection methods and the corresponding iterative image reconstruction via the modified FORBILD phantom

For further validating the performances of these projection methods, we perform two studies on the modified FORBILD phantom [19]. Firstly, we compute the projections via the ordinary, SPLD with re-sampling factors of 2, LIB and DAB pixel-driven projection methods and compare the projection accuracy with the truth being projections generated by use of the Radon function in Matlab. Secondly, we use them in the iterative image reconstruction of the phantom and compare the corresponding reconstruction accuracy. The size of the phantom is 256 × 256. The size of projection set is 256 × 180, meaning that there are 180 uniformly distributed projections from 0° to 179° and there are 256 measurement points on each spatial projection. The sampling pattern is parallel-beam. For the iteration reconstruction, we use the 4 projection methods to calculate the guessed projection in the Chambolle-Pock based least square algorithm (Algorithm 2 in [20]). The measured projection set is simulated by use of the Radon function of Matlab.

Figure 7 shows the projections at angle 45° generated by the 4 projection methods and the corresponding RMSE. It may be clearly seen that the ordinary pixel-driven projection method introduces high-frequency artifact, whereas the proposed 3 new pixel-driven projection methods may generate accurate projections. The intuitive quantitative comparison of the projection-set RMSE is shown in Fig. 8 (a), which shows that the 3 new projection methods achieve lower RMSE, whereas the ordinary pixel-driven has very high error, indicating that use of the method in iterative reconstruction may not lead to high accuracy. Note that, the projection RMSE of SPLD shown in Fig. 8 (a) is much lower than that of LIB and DAB because the reference projection generated by function Radon in Matlab, maybe, comes from projection method similar to SPLD. So it is not reasonable to think that SPLD is much better than LIB and DAB.

Figure 9 shows the reconstructed images. It may be seen that the image reconstructed by use of the ordinary pixel driven projection method suffer from high-frequency line-shape artifacts, whereas the 3 new pixel-driven projection methods may achieve higher accuracy because of their accurate projection calculation. The quantitative RMSE comparison is shown in the second row of Table 1 and Fig. 8 (b), which indicates the same statement, observing that the RMSE of the ordinary pixel-driven projection method is the maximum one.

From Fig. 10, we may see that the central-column-profile reconstructed by use of the ordinary pixel-driven projection method has higher bias compared to the truth. However, the profiles reconstructed by use of SPLD, LIB and DAB method may achieve higher accuracy. The number of projections is 180, thus the system of linear equations modelling the discrete-to-discrete imaging problem is underdetermined. The sparseness radio is $\frac{256\times180}{256\times256} = 70.31\ \%$. So the reconstructions by use of the 3 accurate pixel-driven projection methods still has a certain degree of bias which may be seen form

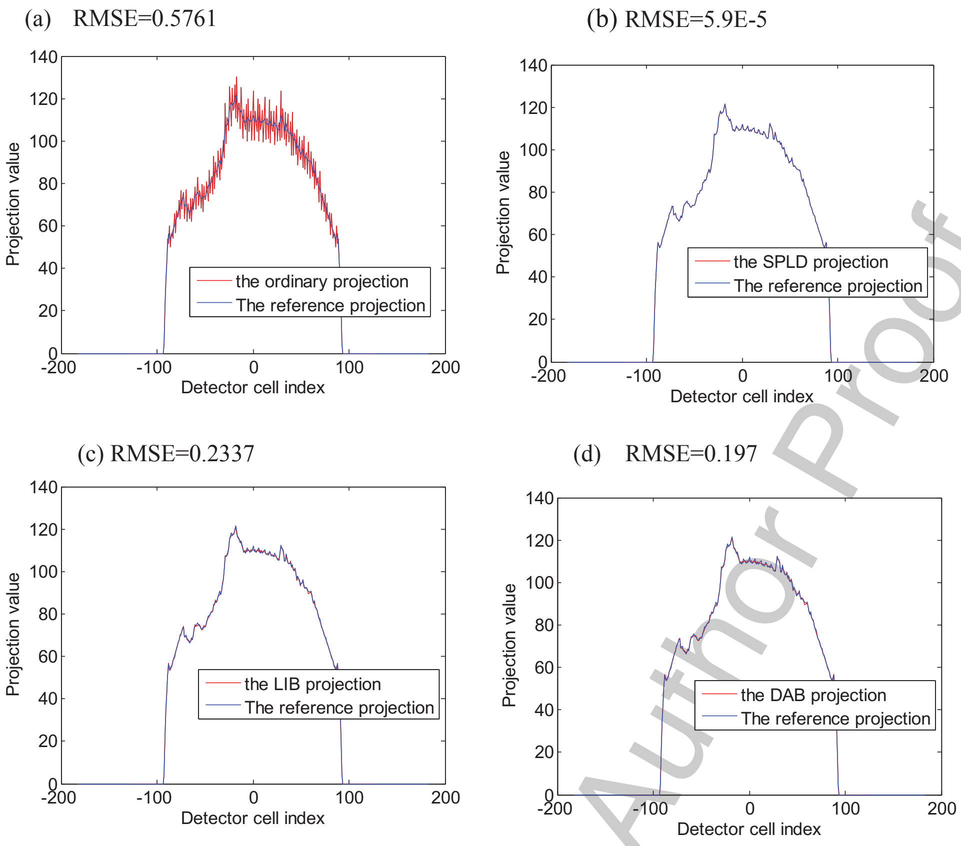

Fig. 7. Projection comparisons at angle 45°. (a) to (d) compares the ordinary, SPLD, LIB and DAB pixel-driven-generated projection with the reference projection by use of Radon function in Matlab.

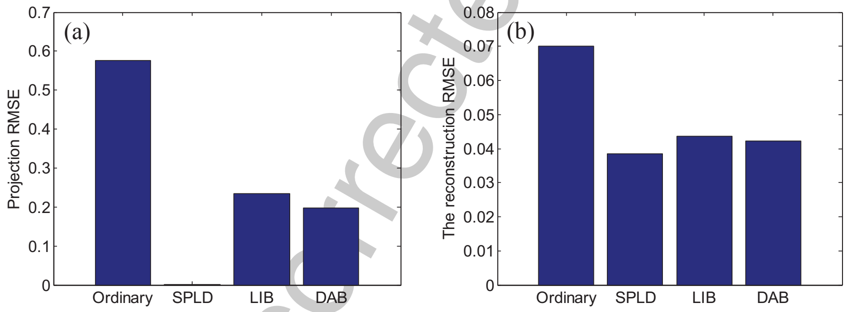

Fig. 8. (a) and (b) are the bar comparisons of the projection RMSE and reconstruction RMSE of the 4 pixel-driven projection methods: ordinary, SPLD, LIB and DAB, respectively.

Fig. 10 (b) to (d). With the increase of number of projections and (or) the use of compressed sensing, the 3 new methods may achieve higher accuracy, however the ordinary pixel-driven method cannot eliminate the high-frequency artifacts because of its inherent disadvantage. For the conciseness, we do not show more evaluations for the reconstructions by use of more projections or use of compressed sensing.

Also, we use another metric, contrast-to-noise (CNR), to evaluate the reconstructions. The signal image is ROI 2 and the background image is ROI 3, which are shown in Fig. 11. The bar comparison

Table 1
Image reconstruction accuracy of the modified FORBILD phantom

	Ordinary pixel-driven	SPLD	LIB	DAB
RMSE	0.0701	0.0384	0.0437	0.0422
CNR	5.6	19.47	14.59	15.71

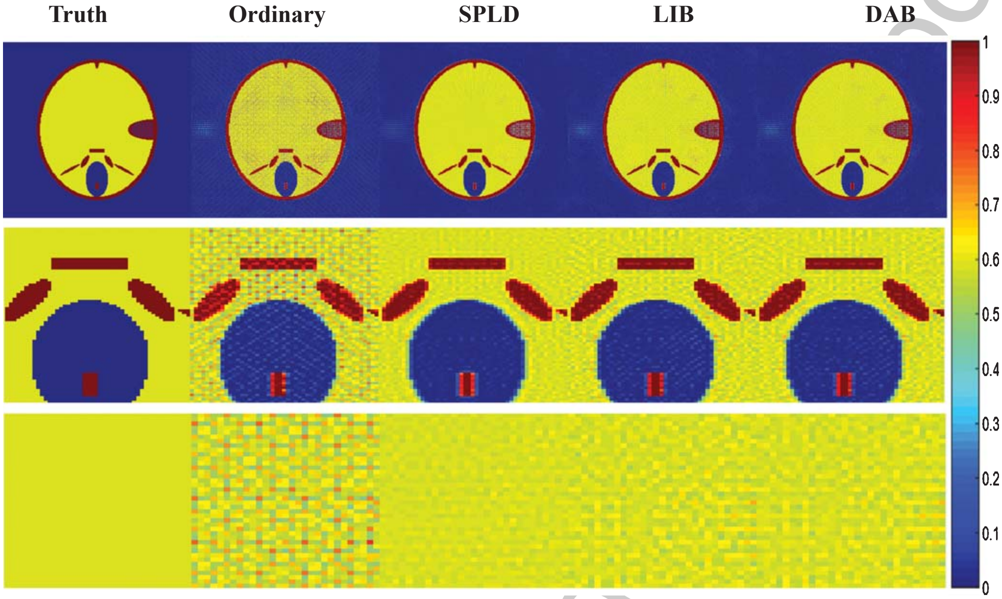

Fig. 9. Comparison of the reconstructed images by use of the 4 pixel-driven projection methods via Chambolle-Pock based least square algorithm. The text above the images indicate the projection method used. The first row shows the whole images; the second and third rows show the images in ROI 1 and 3, respectively. The ROIs are shown in Fig. 10. The display window is [0, 1].

of the CNRs of the ordinary and the 3 proposed projection methods is shown in Fig. 12; the CNR data are shown in Table 1.

From Fig. 12 and the third row of Table 1, we may see that the CNR of the image reconstructed by use of the ordinary projection method is much smaller than the others, indicating that its reconstruction accuracy is lower than the others. The SPLD method achieves the highest CNR, indicating it has the highest accuracy. The conclusion is the consistent with that drawn by analysis of the RMSE metric and the visual evaluations.

All the qualitative and quantitative evaluations consistently indicate that the traditional pixel-driven projection method always generate imprecise projections and certainly lead to imprecise reconstructions and the 3 new projection methods may generate accurate projections and may achieve accurate iterative reconstructions.

3.2. The SPLD pixel-driven projection method for 3D EPRI and its reconstruction quality evaluations

Here, we evaluate the SPLD pixel-driven (in fact, for the 3D case, it may be more accurate to refer to this technique as voxel-driven, but for consistency it will be referred to as a pixel-driven

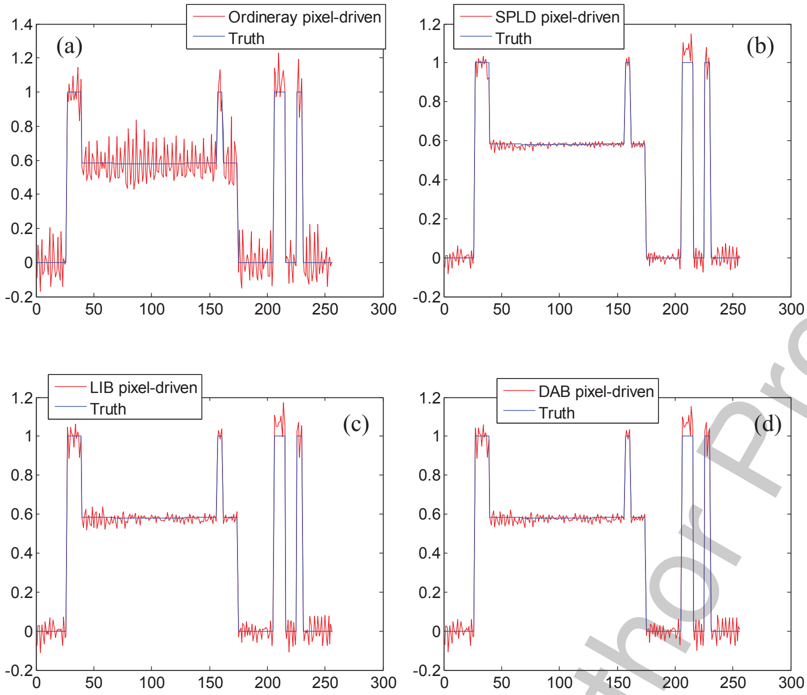

Fig. 10. The central-column profiles comparison of the reconstructed image and the truth FORBILD phantom. (a) to (d) are for the ordinary, SPLD, LIB and DAB pixel-driven projection methods, respectively.

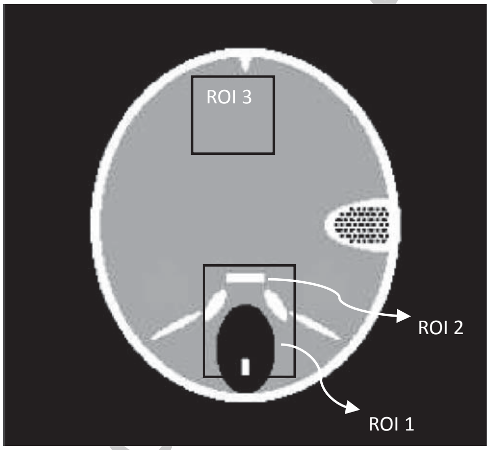

Fig. 11. The ROIs of the modified FORBILD phantom. ROI 1 and 3 are zoomed in and displayed in Fig. 9 to show the details. ROI 3 is used to indicate the background image and ROI 2 the signal image for CNR evaluation. Note that ROI 2 is the pointed white rectangular area.

method) method in 3D EPRI, i.e. 3D inverse Radon transform framework. The 3D voxel grid is of size $64 \times 64 \times 64$ with each voxel being of unit volume. The projection at a specific angle is composed of 64 points with the *virtual* detector cell being of unit length. The rotation center, i.e. the origin of the imaging coordinates system, is located at [32, 32, 32]. The mathematical phantom used is a large sphere containing 5 smaller spheres of varying intensity (Fig. 13).

We use the ordinary pixel-driven method and the SPLD method with re-sampling factor of 2 to generate the projections at a specific angle and compare them with the ideal analytic projection (Fig. 14).

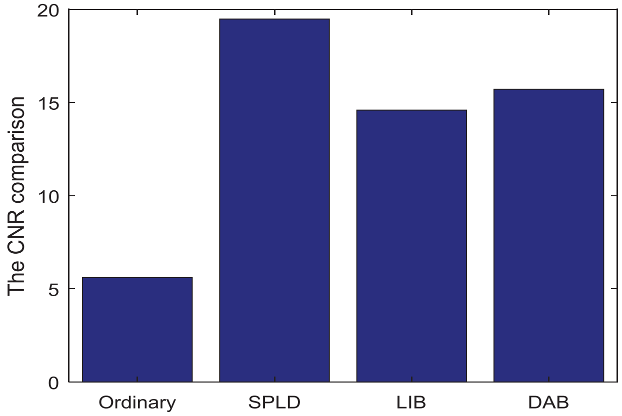

Fig. 12. The CNR comparison of the reconstructed images by use of the 4 pixel-driven projection methods: ordinary, SPLD, LIB and DAB.

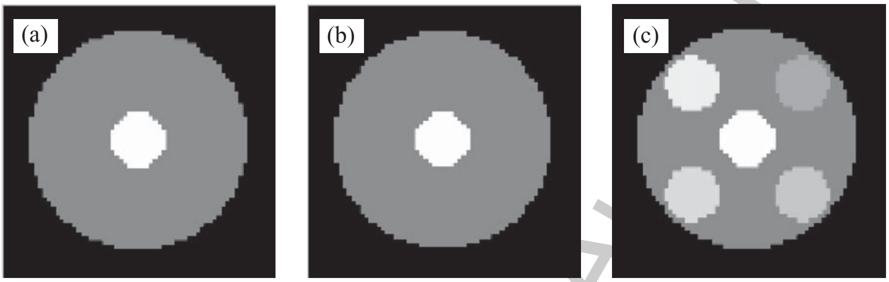

Fig. 13. Image slices of the 3D mathematical phantom. (a) The central *yz*-plane, (b) The central *xz*-plane and (c) The central *xy*-plane.

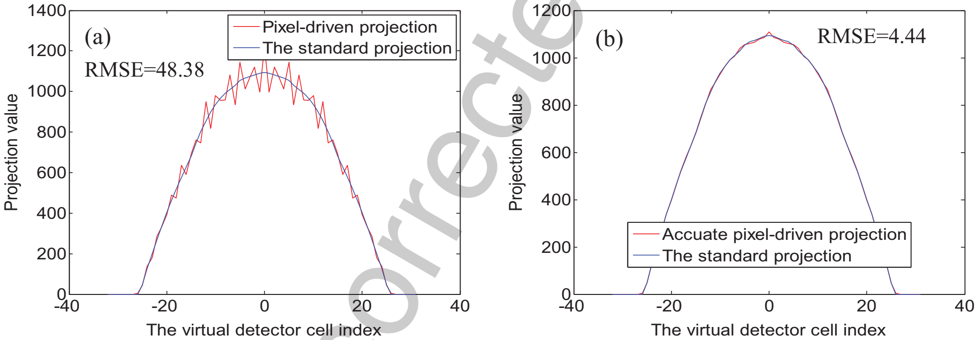

Fig. 14. Comparisons of the traditional and SPLD pixel-driven projection methods. (a) is the comparison of the traditional pixel-driven projection and the analytic projection, regarded as the truth or the standard projection, at a specific angle and (b) is the comparison of the SPLD projection and the truth.

In Fig. 14 (a), it can be seen that the ordinary pixel-driven method results in serious high-frequency artifacts, as evidenced by a very high RMSE of 48.38. However, these artifacts are eliminated when the SPLD pixel-driven method is used (shown in Fig. 14 (b)). Using the SPLD method reduces the RMSE by over an order of magnitude to 4.44.

For the validation that SPLD projection method may achieve accurate iterative reconstruction, we perform several reconstruction studies. The mathematical phantom is what is shown in Fig. 13; the

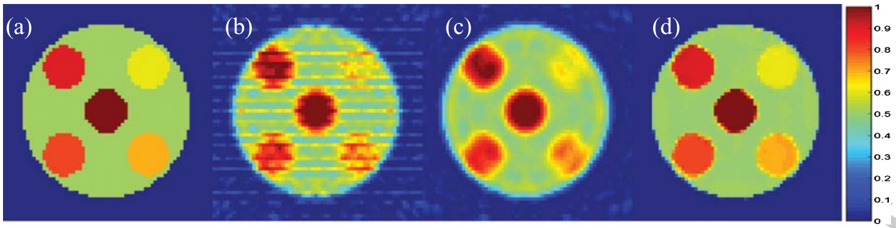

Fig. 15. The central slices of the reconstructed 3D objects. (a) to (d) are for the truth, the objects reconstructed by use of the ordinary and SPLD pixel-driven projection methods via least square algorithm and the object by use of SPLD pixel-driven projection method via TV algorithm, respectively. The display window is [0, 1].

simulated projections are the analytic projections of the mathematical phantom; the size of the object is 64 × 64 × 64; the size of the projection set is 64 × 208, meaning that number of projections is 208 and number of measurements on a virtual spatial projection is 64; the sampling pattern is equal solid angle pattern [20]; the sampling order is Maximally spaced projection sequencing (MSPS) [21].

The iteration algorithm used are the Chambolle-Pock based least square algorithm [20] and total variation (TV)-constrained data-divergence minimization algorithm (it is named as TV algorithm below) [22–24]. In the least square algorithm, the ordinary and SPLD projection methods are used to implement the forward projection operations, respectively. Thus we may evaluate the reconstruction accuracy of the two pixel-driven projection methods. In the TV algorithm, the SPLD is used to implement the forward projection operation. Thus we may further demonstrate the accuracy of SPLD. The iteration number for each reconstruction is 5000 to ensure the convergence.

The central slice-images of the reconstructed 3D object and the truth are shown in Fig. 15. It is clear that the ordinary pixel-driven projection method suffers from severe line-shape artifacts due to the high-frequency artifacts of the forward projection generated by the projection operation during the iteration process. The SPLD pixel-driven method may improve the reconstruction quality. Also, the SPLD method may get more accurate reconstruction by use of compressed sensing or by increase of number of projections. Here, we show the result by use of TV algorithm in Fig. 15 (d), which is visually much more accurate than the use of least square algorithm. The aim for showing the TV result is to illuminate that the reconstruction error of the SPLD based least square algorithm comes from the sparseness of projections sets. In the study, the sparseness radio is $\frac{64\times 208}{64\times 64\times 64} \approx 5.1\,\%$, which is too sparse for least square algorithm to achieve accurate reconstruction. If the ordinary pixel-driven projection method is used, the reconstruction artifacts cannot be avoided even more projections or compressed sensing techniques are used. But we do not show more reconstruction results for the briefness.

Figure 16 shows the RMSE and profile comparisons for the study. It may be seen from Fig. 16 (a) and the second row of Table 2 that the ordinary pixel-driven projection method has the highest RMSE, however the SPLD method may achieve higher accuracy (lower RMSE). Comparing Fig. 16 (b) and (c), we may see that the profiles reconstructed by use of the ordinary pixel-driven projection method suffer from higher bias. The SPLD method may suppress the bias. If regularization technique is used, for example TV minimization, the reconstruction accuracy may be higher (see Fig. 16 (d) and its RMSE value shown in Fig. 16 (a)). Also, we use CNR to continue evaluate the reconstruction accuracy. The signal ROI and the background ROI are shown in Fig. 17 (a). The CNR bar comparison is shown in Fig. 17 (b) and the CNR data are shown in Table 2.

From Fig. 17 (b) and the third row of Table 2, we see that the SPLD pixel-driven projection method may outperform the ordinary projection method as per the CNR evaluation on the reconstructed object. Here, the CNR of the ordinary method is just 3.88. However, CNR of the SPLD method has increased to 11.58. If we use TV algorithm with the use of SPLD projection method, the CNR may achieve very high value as 460.95.

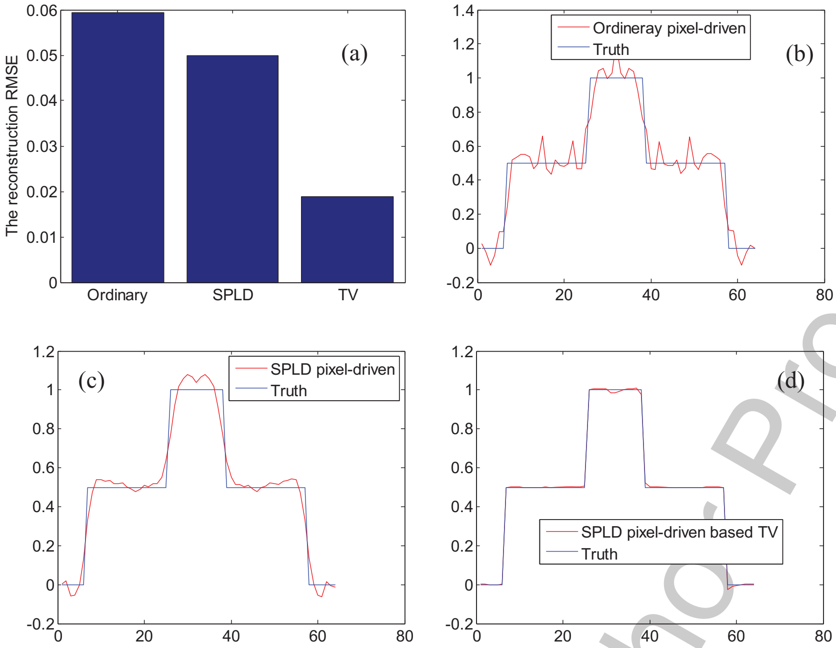

Fig. 16. (a) is for bar-comparisons of the reconstruction RMSE of the ordinary, SPLD pixel-driven based least square algorithm and SPLD pixel-driven based TV algorithm. (b) to (d) are for the profile- comparisons of the three cases and the truth, respectively.

Table 2
Image reconstruction accuracy of 3D EPRI

	Ordinary pixel-driven based LS	SPLD based LS	SPLD based TV
RMSE	0.0594	0.0498	0.0189
CNR	3.88	11.58	460.95

In summary, both the qualitative and the quantitative evaluations appear to illuminate that the SPLD projection method may be used in iterative reconstruction algorithms for 3D EPRI to achieve high accuracy; however the ordinary pixel-driven projection method always suffers from high-frequency artifacts, confining its application.

4. Discussion and conclusion

In iterative image reconstruction algorithms, projection and backprojection are the two most important and frequently used operations. The former calculates a projection from an iteration of the image being reconstructed to evaluate the projection residual (difference between calculated projection and the measured projection). The latter updates the image by back-distributing the residual.

In this work, we focus on accurate projection methods for iterative reconstruction. We propose 3 novel accurate pixel-driven projection methods: SPLD, LIB and DAB pixel-driven methods. Then we verified, evaluated and compared the 3 methods performance in 2D CT. We found that all the 3 methods have yielded accurate projections and reconstructions and rectified the issues associated with the ordinary pixel-driven projection methods that are known to result in high-frequency artifacts.

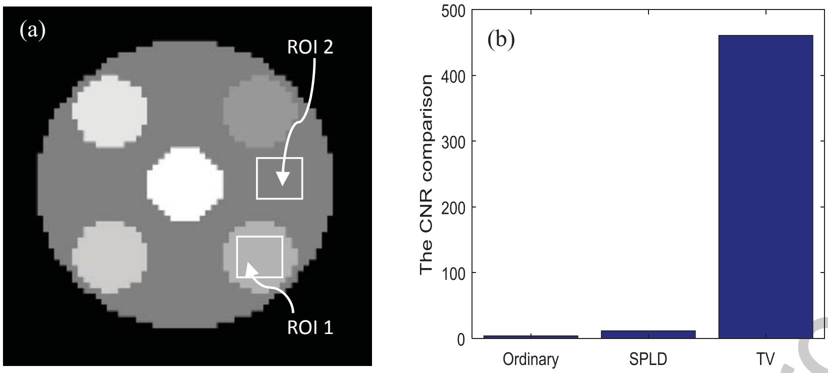

Fig. 17. (a) the slice of the 3D phantom and the ROI area for CNR evaluation. (b) the CNR bar comparison of reconstructed objects by use of the ordinary and SPLD projection method in least square algorithm and the SPLD method in TV algorithm.

We also extend the SPLD pixel-driven method to 3D EPR imaging. The projection generated from a 3D object using SPLD pixel-driven method with a re-sampling factor ≥ 2 showed an immense improvement in projection accuracy and the corresponding reconstruction accuracy compared to the ordinary pixel-driven method.

The SPLD pixel-driven projection methods need to divide each pixel into 4 small pixels (or each voxel into 8 small voxels) if re-sampling factor of 2 is used. Thus the projection operation will become slower. By the use of graphic processing unit (GPU), the disadvantage may be ignored. Another possible disadvantage will come out if the SPLD method is used in divergent beam CT. For example, in fan-beam CT, if we use SPLD, the appropriate weighting factor should be well designed and used to adapt it to the different magnification times for the different pixels.

While the motivation of this work was to investigate effective methods for the calculation of projections in 3D and 4D EPRI, this work may also be relevant to other imaging modalities. The pixel-driven projection methods have certain characteristics that make them particularly versatile as far as application across different imaging modalities: simple principle, no sub-classification of row- and column-action implementations, simple mathematical assumptions (pixels and detector cells are both points), high degree of parallelization, and they are readily extended to different dimensionalities, geometries, etc. In the future, these new methods may be further investigated and could be easily adapted for use in other medical imaging modalities.

Acknowledgments

The authors would like to thank Drs. Zheng Zhang of the University of Chicago, Tianye Niu of Zhejiang University, Wei Zhao of Huazhong University of Science and Technology, Shaojie Tang of Xi'an University of Posts and Telecommunications for their valuable discussions. This work was supported in part by the Natural Science Foundation of Shanxi Province under grant 201601D011041, by the National Institutes of Health (NIH) under grants P41 EB002034 and R01 CA98575 and R50 CA211408-01 and by the China Scholarship Council under grant 201608140014.

References

[1] A.G. Christodoulou, et al., Fast dynamic electron paramagnetic resonance (EPR) oxygen imaging using low-rank tensors, *Journal of Magnetic Resonance* **270** (2016), 176–182.

[2] Z. Qiao, et al., 3D pulse EPR imaging from sparse-view projections via constrained, total variation minimization, *Journal of Magnetic Resonance* **258** (2015), 49–57.

[3] G.L. Zeng and G. Gullberg, Ray-driven backprojector for backprojection filtering and filtered backprojection algorithms. in Publ by IEEE; 1994.

[4] A.H. Ahn and H.J. Halpern, Simulation of 4D spectral-spatial EPR images, *Journal of Magnetic Resonance* **187**(1) (2007), 1–9.

[5] K.H. Ahn and H.J. Halpern, Spatially uniform sampling in 4-D EPR spectral-spatial imaging, *Journal of Magnetic Resonance* **185**(1) (2007), 152–158.

[6] T. Peters, Algorithms for fast back-and re-projection in computed tomography, *IEEE Transactions on Nuclear Science* **28**(4) (1981), 3641–3647.

[7] H. Gao, Fast parallel algorithms for the x-ray transform and its adjoint, *Medical Physics* **39**(11) (2012), 7110–7120.

[8] R.L. Siddon, Fast calculation of the exact radiological path for a three-dmensional CT array, *Medical Physics* **12**(2) (1985), 252–255.

[9] P.M. Joseph, An improved algorithm for reprojecting rays through pixel images, *IEEE Transactions on Medical Imaging* **1**(3) (1982), 192–196.

[10] M. Ertas, et al., Iterative image reconstruction using non-local means with total variation from insufficient projection data, *Journal of X-ray Science and Technology* **24**(1) (2016), 1–8.

[11] B. De Man and S. Basu, Distance-driven projection and backprojection in three dimensions, *Physics in Medicine and Biology* **49**(11) (2004), 2463.

[12] B.D. Man and S. Basu, Distance-driven projection and backprojection, *in Nuclear Science Symposium Conference Record* 2002 IEEE. 2002. IEEE.

[13] C. Jian-Lin, et al., Fast parallel algorithm for three-dimensional distance-driven model in iterative computed tomography reconstruction, *Chinese Physics B* **24**(2) (2015), 028703.

[14] G.L. Zeng and G.T. Gullberg, Unmatched projector/backprojector pairs in an iterative reconstruction algorithm, *IEEE Transactions on Medical Imaging* **19**(5) (2000), 548–555.

[15] Y. Long, J.A. Fessler and J.M. Balter, 3D forward and back-projection for X-ray CT using separable footprints, *IEEE Transactions on Medical Imaging* **29**(11) (2010), 1839–1850.

[16] M. Zwicker, et al., EWA splatting, *IEEE Transactions on Visualization and Computer Graphics* **8**(3) (2002), 223–238.

[17] J. Bian, et al., Evaluation of sparse-view reconstruction from flat-panel-detector cone-beam CT, *Physics in Medicine and Biology* **55**(22) (2010), 6575.

[18] Z. Qiao, et al., Comparison of parabolic filtration methods for 3D filtered back projection in pulsed EPR imaging, *Journal of Magnetic Resonance* **248** (2014), 42–53.

[19] Z. Yu, et al., Simulation tools for two-dimensional experiments in x-ray computed tomography using the FORBILD head phantom, *Physics in Medicine and Biology* **57**(13) (2012), N237.

[20] E.Y. Sidky, J.H. Jørgensen and X. Pan, Convex optimization problem prototyping for image reconstruction in computed tomography with the Chambolle–Pock algorithm, *Physics in Medicine and Biology* **57**(10) (2012), 3065.

[21] G. Redler, B. Epel and H.J. Halpern, Maximally spaced projection sequencing in electron paramagnetic resonance imaging, *Concepts in Magnetic Resonance Part B: Magnetic Resonance Engineering* **45**(1) (2015), 33–45.

[22] Z. Zhang, et al., Artifact reduction in short-scan CBCT by use of optimization-based reconstruction, *Physics in Medicine and Biology* **61**(9) (2016), 3387.

[23] D. Xia, et al., Optimization-based image reconstruction with artifact reduction in C-arm CBCT, *Physics in Medicine and Biology* **61**(20) (2016), 7300.

[24] Z. Zhang, et al., Investigation of optimization-based reconstruction with an image-total-variation constraint in PET, *Physics in Medicine and Biology* **61**(16) (2016), 6055.

Appendix: SPLD pixel-driven projection program in Matlab.

```
%    This program calculates projections using the newly developed SPLD pixel-driven method. The
%    re-sampling factor may be arbitrarily set to any number. If the factor is set to be 1, then the program
%    is equivalent to the traditional pixel-driven projection method, which results in high-frequency
%    artifacts.

ImageLength=256;          % size of the image
numProj=12;    % number of projections equally spaced in the range of  [0^o,180^o].
object=phantom(ImageLength);       % here the object is the Shepp-Logan phantom.
factor=2;          % re-sampling factor 3 means each pixel is divided into 9 sub-pixels of equal size.
s=0:factor-1;             % s is the index corresponding to the sub-pixels.
startPoint=-0.5+0.5*1/factor;
s=startPoint+s*(1/factor);
center= floor((ImageLength+1)/2);           % the origin of the imaging coordinates system
proj=zeros(ImageLength,numProj);                   % the projection.
for jj=1:numProj
    theta=((jj-1)*180/numProj)*pi/180;
    for m=1:ImageLength
        for n=1:ImageLength
            x=n-center;
            y=center-m;
            for iii=1:factor
                for jjj=1:factor
                    t=(x+s(iii))*cos(theta)+(y+s(jjj))*sin(theta);
                                % to calculate the projecting address
                    if t>=(-ImageLength/2)&&t<=ImageLength/2-1;
                        tleft=floor(t);
                        tright=ceil(t);
                        if tleft~=tright            % to judge if the projecting address is located
                                                    % between two detector-cell-points.
                            left_dis=t-tleft;
                            right_dis=tright-t;
                             proj(centerN+tleft,jj)=proj(centerN+tleft,jj)+object(m,n)*(right_dis)/
                             factor^2;          % note the use of factor
                             proj(centerN+tright,jj)=proj(centerN+tright,jj)+object(m,n)*(left_dis)
                             /factor^2;
                        else
                            proj(centerN+tleft,jj)=proj(centerN+tleft,jj)+object(m,n)/factor^2;
                        end
                    end
                end
            end
        end
    end
end
theta2=0:180/numProj:180-180/numProj;          % projection angles
[proj_radon,proj_x2]=radon(object,theta2);      % note the use of built-in Matlab radon function
proj_x1=-center:1:center-1;                    % detector cell index
figure;            % visual comparison of the projections calculated using the SPLD method
                   % and radon function
for ii=1:numProj
    plot(proj_x1,proj(:,ii),'r',proj_x2,proj_radon(:,ii),'b');
    xlabel('The detector cell index');
    ylabel('Projection value');
    title(['Comparison of accurate pixel-driven with radon function:',num2str((ii-1)*180/numProj)]);
    legend('Pixel-driven projection','System projection');
    drawnow;
    pause(0.1);
end
```